ChemEngineering

MDPI

Article

Structure-Based Screening and Molecular Dynamics of Rifampicin Analogues Targeting *InhA* of *Mycobacterium tuberculosis*

Lucas Paul [1,*] and Andrew S. Paluch [2,*]

[1] Department of Chemistry, Dar es Salaam University College of Education, Dar es Salaam P.O. Box 2329, Tanzania
[2] Department of Chemical, Paper and Biomedical Engineering, Miami University, Oxford, OH 45056, USA
* Correspondence: lucas.paul@udsm.ac.tz (L.P.); paluchas@miamioh.edu (A.S.P.)

Abstract

Tuberculosis (TB), caused by *Mycobacterium tuberculosis* (Mtb), remains a global health burden, particularly due to multidrug-resistant (MDR) and extensively drug-resistant (XDR) strains. Rifampicin, a frontline anti-TB drug that inhibits RNA polymerase, has been central to therapy, but *rpoB* mutations compromise its efficacy. This highlights the need for Rifampicin analogues that target alternative enzymes to sustain therapeutic effectiveness. In this study, a structure-based computational approach was employed to screen Rifampicin analogues against enoylacyl carrier protein reductase (*InhA*), a validated enzyme in the biosynthesis of mycolic acids. A library of 399 analogues was retrieved from SwissSimilarity and evaluated using ADMET analysis, with the best candidates showing favourable pharmacokinetic profiles and compliance with Lipinski's Rule of Five. Molecular docking identified ZINC000013629834 (−10.90 kcal/mol) and ZINC000253411694 (−10.36 kcal/mol) as superior to Rifampicin (−9.05 kcal/mol), with ILE21, SER20, and THR196 consistently stabilizing interactions. Molecular dynamics simulations confirmed the stability of the complexes, with RMSD values of 0.167 nm, 0.175 nm, and 0.297 nm for ZINC000013629834, ZINC000253411694, and Rifampicin, respectively. MM/PBSA analysis showed comparable binding free energies. These findings suggest that optimized Rifampicin analogues targeting *InhA* may overcome *rpoB*-associated resistance and serve as promising leads for next-generation anti-TB drug development.

Keywords: tuberculosis; multidrug resistant; molecular docking; molecular dynamics; pharmacokinetics

Check for updates

Academic Editors: Nicoleta Nicole Radu and Amalia Stefaniu

Received: 2 October 2025
Revised: 11 January 2026
Accepted: 26 January 2026
Published: 6 February 2026

Copyright: © 2026 by the authors. Licensee MDPI, Basel, Switzerland. This article is an open access article distributed under the terms and conditions of the Creative Commons Attribution (CC BY) license.

1. Introduction

Tuberculosis (TB), caused by the intracellular pathogen *Mycobacterium tuberculosis* (Mtb), continues to pose a formidable public health threat [1]. Despite being a preventable and curable disease, TB remains one of the top 10 causes of death globally and the leading cause from a single infectious agent [2]. According to the World Health Organization (WHO), in 2023 alone, over 10 million people developed active TB, and approximately 1.3 million succumbed to the disease [3–6]. These numbers highlight the persistent burden of TB in both high and low-income countries, compounded by socioeconomic inequalities, limited access to healthcare, and diagnostic challenges.

Beyond active disease, the burden of latent tuberculosis infection (LTBI) is even more profound. As of 2014, it was estimated that nearly 1.7 billion people, roughly 23% of the

world's population, harboured LTBI [7,8]. This silent reservoir poses a constant threat to TB control efforts, as approximately 5–10% of infected individuals may progress to active disease in their lifetime [9]. The majority of individuals with LTBI are concentrated in resource-limited regions, particularly in Africa, Southeast Asia, and the Western Pacific, where 80% of cases are found and where TB transmission remains high due to weak healthcare infrastructure and coinfections such as HIV [10,11]. While conventional first-line anti-TB drugs, including isoniazid, Rifampicin, ethambutol, and pyrazinamide, have been effective in combating drug-sensitive TB, the emergence and spread of multidrug-resistant (MDR-TB) and extensively drug-resistant (XDR-TB) strains have significantly undermined global progress [12,13]. MDR-TB is defined as resistance to at least isoniazid and Rifampicin, the two most potent TB drugs [14]. At the same time, XDR-TB includes resistance to fluoroquinolones and second-line injectable agents [15]. These forms of drug resistance demand longer, more toxic, and less effective treatment regimens, often with poor treatment outcomes and increased economic burden.

Consequently, there is an urgent need for novel anti-tubercular compounds with new mechanisms of action, favourable pharmacological profiles, and low resistance potential [16]. Rifampicin resistance in *M. tuberculosis* primarily results from mutations within the rpoB gene, which alter the Rifampicin-binding site on RNA polymerase and prevent effective drug engagement. In contrast, *InhA* remains structurally conserved in Rifampicin-resistant isolates, making it an attractive alternative therapeutic target. Redirecting rifamycin-derived analogues toward *InhA* therefore represents a mechanistically distinct strategy that may circumvent rpoB-mediated resistance while retaining desirable pharmacological features of the parent scaffold.

Since ancient times, natural products have played a cornerstone role in antimicrobial discovery, contributing to nearly 60% of existing antibiotics [17]. For instance, streptomycin, the first anti-tuberculosis drug, was derived from a natural source [18]. These bioactive compounds have provided crucial scaffolds for the development of clinically viable therapeutics. The remarkable chemical diversity of natural products, spanning both terrestrial and marine ecosystems, continues to inspire the search for novel agents. Today, researchers leverage this wealth of information to explore chemical space and design or identify new analogues of known drugs [19,20].

The traditional drug discovery process, though effective, is often time-consuming, costly, and characterized by high attrition rates. In recent years, the integration of computational approaches has significantly enhanced early-stage drug development by enabling rapid virtual screening, target prioritization, and lead optimization. In silico techniques such as molecular docking, pharmacokinetic profiling (ADMET), and molecular dynamics (MD) simulations allow for the detailed evaluation of protein-ligand interactions, absorption, distribution, metabolism, excretion, and toxicity critical parameters in the selection of drug-like molecules [21–23]. These tools not only reduce the cost and duration of the discovery pipeline but also improve accuracy by mimicking biological environments and molecular behaviour over time.

Moreover, combining molecular docking with MD simulations provides valuable insight into the dynamic behavior and stability of protein-ligand complexes under physiological conditions. Meanwhile, ADMET profiling helps to rule out compounds with poor oral bioavailability or high toxicity early in the process, increasing the likelihood of downstream success. Together, these computational strategies form a robust framework for rational drug design and are particularly suited for screening large natural product libraries.

In this study, we harness a comprehensive in silico drug discovery pipeline to investigate the anti-tubercular structural analogues of Rifampicin. Specifically, we targeted *InhA* (enoyl-acyl carrier protein reductase) of *M. tuberculosis*, a key enzyme in the FAS-II mycolic

acid biosynthesis pathway and the primary protein used for structure-based screening in this study. Through the integration of molecular docking, pharmacokinetic modelling, and molecular dynamics simulations, this research seeks to uncover promising rifampicin analogues that could serve as leads for future anti-TB drug development. Our findings not only expand the chemical space for TB therapeutics but also support the growing interest in natural products as a rich and untapped source of new pharmacophores.

This study presents an early-stage computational screening designed to identify Rifampicin analogues with potential inhibitory activity against *InhA*. The resulting hit compounds offer a basis for future biochemical and biophysical validation.

2. Materials and Methods

2.1. Receptor Structure Preparation

The three-dimensional X-ray crystallographic structure of enoylacyl carrier *Mycobacterium tuberculosis* protein reductase (*InhA*), complexed with its native cofactor NADH and the inhibitor isoniazid (PDB ID: 2IDZ), was obtained from the RCSB Protein Data Bank [24]. The co-crystallized ligand positioned within the active site was utilized to guide the identification of the binding pocket for virtual screening purposes. For computational efficiency, only chain A of the protein was retained, while additional chains, water molecules, and heteroatoms were excluded. The protein structure was converted from PDB to PDBQT format using MGLTools v1.5.7 [25] to facilitate docking simulations. UCSF ChimeraX 1.4 [26] was further used to pre-process and refine the receptor structure for downstream molecular dynamics simulations, ensuring the removal of unwanted residues and the proper assignment of bond orders and hydrogen atoms.

2.2. Ligand Structure Preparation

A library of 400 drug-like compounds, including Rifampicin as the reference standard (gold standard), was retrieved from the SwissSimilarity platform [27] http://www.swisssimilarity.ch/ (accessed on 10 August 2025) based on structural similarity to known anti-tubercular agents. The compounds were downloaded in SDF format and subsequently energy-minimized using Open Babel (obabel) v3.1.1 [28] with the Merck Molecular Force Field (MMFF94) [29] to obtain geometrically stable conformations [30]. Following minimization, the structures were converted to PDBQT format by assigning Gasteiger charges and defining rotatable bonds and torsional degrees of freedom. To ensure drug likeness, all compounds were evaluated against Lipinski's Rule of Five, which states that orally active drugs generally comply with the following criteria: molecular weight $\leq$ 500 Da, logP $\leq$ 5, no more than 5 hydrogen bond donors, and no more than 10 hydrogen bond acceptors [31]. Compounds violating more than one criterion were excluded from further docking analysis.

2.3. Evaluation of the Drug-Likeness Properties of Selected Compounds

The evaluation of drug similarity properties of candidate compounds is a fundamental component of early phase drug discovery, as it provides critical information on their potential pharmacokinetic behaviour in vivo [32]. While strong binding affinity and target-specific inhibitory activity are essential characteristics of lead compounds, they do not guarantee success in drug development. Many promising molecules fail in later stages due to suboptimal physicochemical or pharmacokinetic properties, such as poor absorption, low bioavailability, or metabolic instability. Drug-likeness screening helps eliminate such compounds early in the pipeline, thereby improving the efficiency and success rate of downstream optimization efforts. In this study, a total of 399 small molecules structurally similar to Rifampicin, a well-established antitubercular drug, were retrieved from the SwissSimi-

larity platform. Rifampicin was included as a reference compound to benchmark structural and pharmacological characteristics. All compounds were subjected to drug similarity evaluation using the SwissADME online tool [33] (http://www.swissadme.ch/index.php, accessed on 11 August 2025), which calculates a range of commonly used descriptors in medicinal chemistry. Specifically, the evaluation focused on molecular weight (MW), hydrogen bond donors (HBD), hydrogen bond acceptors (HBA), and lipophilicity expressed as MLOGP. These parameters are recognized as key indicators of a compound's oral bioavailability and its ability to reach and remain at therapeutic concentrations at the site of action [33]. Additionally, all compounds were screened according to Lipinski's Rule of Five, a widely accepted set of criteria developed by Pfizer to estimate the drug-likeness and oral bioavailability of small molecules [34]. Compounds that violated more than one of these rules were excluded from further analysis to increase the likelihood of identifying candidates with favourable pharmacokinetic properties. This filtration step was crucial in streamlining the compound library for molecular docking and subsequent dynamic simulations, ensuring that only the most promising candidates with drug-like characteristics were advanced for structure-based screening against *Mycobacterium tuberculosis* targets. The integration of drug-likeness profiling at this stage strengthens the reliability of computational drug discovery workflows and enhances the translational potential of identified hits.

2.4. ADMET Profiling

The selected compounds were evaluated for their pharmacokinetic and toxicity profiles using the pkCSM web-based (http://biosig.lab.uq.edu.au/pkcsm/prediction accessed on 11 August 2025) platform [32]. This analysis encompassed key ADMET parameters, including gastrointestinal (GI) absorption, blood–brain barrier (BBB) permeability, central nervous system (CNS) bioavailability, and potential as a substrate or inhibitor of P-glycoprotein. In addition, cytochrome P450 enzyme interactions, specifically with CYP3A4 and CYP2D6 isoforms, were assessed to predict possible metabolic liabilities and drug–drug interaction risks. Elimination-related properties, such as total clearance (mL/min/kg), renal OCT2 transporter inhibition, and mutagenicity (based on the Ames test), were also examined to further evaluate compound disposition and genetic safety. Toxicological endpoints critical to human safety, including the potential to inhibit the hERG potassium channel (a key predictor of cardiotoxicity), likelihood of hepatotoxicity, and dermal sensitization potential, were systematically analyzed. These in silico predictions served as an essential early-stage filter to identify and exclude compounds with undesirable pharmacokinetic or toxicological characteristics, thereby prioritizing those with favourable drug-like profiles for further computational and experimental investigation.

2.5. Molecular Docking

The molecular docking study proceeded by defining the binding site based on the location of the native ligand within the crystal structure. A grid box was generated around the predicted active site using MGLTools v1.5.7 [25], with its centre set at coordinates x = −6.07 Å, y = 2.87 Å, and z = 22.63 Å. The dimensions of the grid were specified as 50 Å (*x*-axis), 60 Å (*y*-axis), and 50 Å (*z* axis), ensuring complete coverage of the binding pocket. The docking simulations were performed using AutoDock Vina v1.2.3 [35], with the exhaustiveness parameter set to 10 and a grid spacing of 1.0 Å to balance speed and accuracy. The resulting binding poses were analyzed using BIOVIA Discovery Studio Visualizer 2021 v2021.1 [36] and UCSF ChimeraX 1.4 [37]. Compounds demonstrating strong binding affinities and favourable interaction profiles see (Table 1), within the active site were shortlisted for subsequent molecular dynamics simulations.

Table 1. Molecular docking scores of the top ten virtually screened compounds from the ZINC database [38], Native ligand and the reference compound Rifampicin.

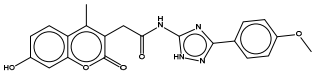
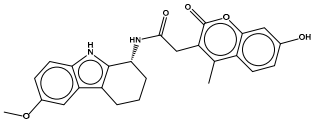
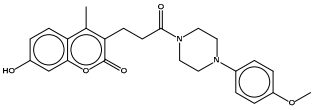
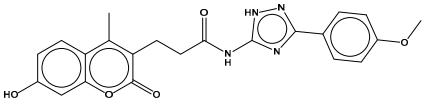
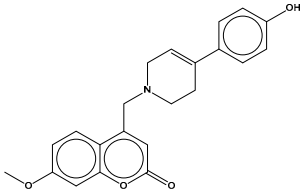
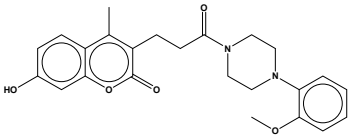
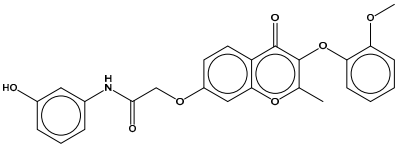
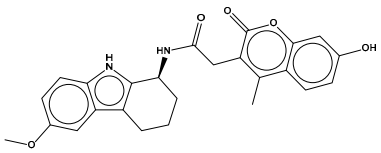
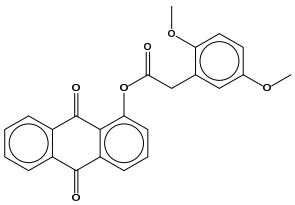
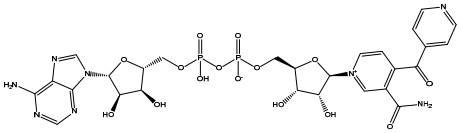
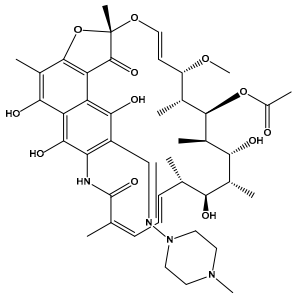
Compound	Binding Energy (Kcal/Mol)	Structures
ZINC000013629834	−10.90	
ZINC000253411694	−10.36	
ZINC000009418955	−10.33	
ZINC000009306325	−10.31	
ZINC000032851106	−10.21	
ZINC000009304208	−10.08	
ZINC000009548024	−9.81	
ZINC000253411693	−9.76	
ZINC000007039726	−9.75	
Native ligand	−9.38	

Table 1. *Cont.*

Compound	Binding Energy (Kcal/Mol)	Structures
Rifampicin	−9.05	

2.6. Molecular Dynamics Simulation

Following molecular docking, the top two-ranked protein–ligand complexes (see Table 1) plus Rifampicin were subjected to molecular dynamics (MD) simulations using GROMACS 2018 [39]. Protein topology files were generated with the pdb2gmx utility, while ligand parameters were derived from the SwissParam server (accessed 16 August 2025) [40,41] to ensure compatibility with the CHARMM36 force field [42]. The processed protein and ligand structures were combined to form complete complex systems. Each system was placed in a cubic simulation box with a minimum margin of 1.0 nm from any box edge and solvated with explicit TIP4P water molecules [43]. Before the production run, energy minimization was carried out using the steepest descent algorithm (500 steps) to remove steric clashes and optimize system geometry. The minimized systems underwent a two-phase equilibration process: (i) constant number of particles, volume, and temperature (NVT) equilibration at 300 K using the V-rescale (stochastic velocity rescaling) thermostat [44], followed by (ii) constant number of particles, pressure, and temperature (NPT) equilibration at 1 bar using the Parrinello-Rahman barostat [45] with the V-rescale thermostat. The NVT and NPT phases were run for 250 ps and 500 ps, respectively, with positional restraints applied to protein and ligand heavy atoms, allowing solvent molecules to equilibrate freely. Long-range electrostatics were computed using the Particle Mesh Ewald (PME) method [46], and covalent bond constraints involving hydrogen atoms were applied via the LINCS algorithm [47]. The production MD simulations were performed for 100 ns with a 2 fs integration time step, recording trajectory frames every 1 ps without restraints. Post-simulation analyses included evaluation of structural and dynamic parameters: root mean square deviation (RMSD) of Cα atoms, root mean square fluctuation (RMSF) of residues, radius of gyration (Rg), intermolecular hydrogen bond profiles, Solvent Accessible Surface Area (SASA) and construction of the free energy landscape (FEL) for each complex.

2.7. Free Energy Landscapes

To evaluate the conformational stability, flexibility, and atomic motions of the *InhA* protein and its ligand-bound complexes, we performed a principal component analysis (PCA) to investigate their essential dynamics [48]. PCA was also used to construct free energy landscapes (FELs) of *InhA* in the apo and complex states by applying a conformational sampling approach [49]. These FELs facilitated the identification of conformations closer to the native state and were used to assess the stability and native-like configurations of *InhA* before and after ligand binding.

2.8. Molecular Mechanics Poisson–Boltzmann Surface Area (MM/PBSA) Analysis

The Molecular Mechanics Poisson–Boltzmann Surface Area (MM/PBSA) method is a widely used computational approach for estimating the binding free energy of biomolecule complexes, particularly protein–ligand interactions that are not fully captured by molecular docking [50,51]. This method combines molecular mechanics energy terms with implicit solvent models to provide insights into the thermodynamic contributions governing molecular recognition and binding. In the present study, the *g_mmpbsa* tool was employed to calculate the binding free energies of *InhA* in complex with ZINC000013629834, ZINC000253411694, and Rifampicin, according to the following equations:

$$\Delta G_{binding} = G_{complex} - G_{protein} + G_{ligand} \quad (1)$$

$$G_x = E_{MM} + G_{sol} - TS \quad (2)$$

$$E_{MM} = E_{bonded} + E_{nonbonded} = E_{bonded} + (E_{vdW} + E_{elec}) \quad (3)$$

$$G_{sol} = G_{polar} + G_{nonpolar} = G_{polar} + (\gamma \cdot S\ AS\ A + b) \quad (4)$$

Here, $G_{complex}$, $G_{protein}$, and G_{ligand} represent the free energies of the complex, protein, and ligand, respectively. In Equation (2), the subscript x denotes the system under consideration (protein, ligand, or complex). E_{MM} is the average molecular mechanics energy in vacuum, while TS is the entropic contribution (T = absolute temperature, S = entropy). Since entropy calculations are computationally demanding, this term was omitted in the *g_mmpbsa* implementation.

Equation (3) separates molecular mechanics energies into bonded and nonbonded components, with the latter including both van der Waals (E_{vdW}) and electrostatic (E_{elec}) interactions. The solvation free energy (G_{sol}) in Equation (4) was determined using an implicit solvent model, which includes polar and nonpolar contributions. The nonpolar term was estimated using the solvent-accessible surface area (SASA), where γ is the surface tension proportionality constant (set to 0.0072 kcal·mol^{-1}·Å^{-2}) and b is the nonpolar solvation parameter (set to 0.00 kcal·mol^{-1}) as also described by [52]. A total of 200 snapshots were evenly extracted from the molecular dynamics trajectories and used to compute the binding free energies of the protein–ligand complexes.

3. Results

3.1. Docking Validation and Benchmarking

To validate the robustness and reliability of the docking protocol employed in this study, a benchmarking from experimental data and re-docking strategy was adopted using previously reported binding energy data that used the same approach. These literature data provide an appropriate reference framework for methodological validation. First, reproduce the experimental values obtained from the isothermal titration calorimetry (ITC) [53], we used targets and inhibitors used to their study to reproduce using molecular docking by AutoDock vina v1.2.3 as presented in Figure 1 and Table S1, with a strong correlation of $R^2 = 0.83$.

In addition, a re-docking validation was performed using a highly cited molecular docking study that employed AutoDock Vina v1.2.3 as the primary scoring function [54]. The docking protocol described in this reference was reproduced using identical AutoDock Vina v1.2.3 settings. The re-docked ligand poses showed good agreement with the reported docking conformations, and the reproduced docking scores exhibited a very strong correlation with the published values ($R^2 = 0.94$; Figure S1 and Table S2).

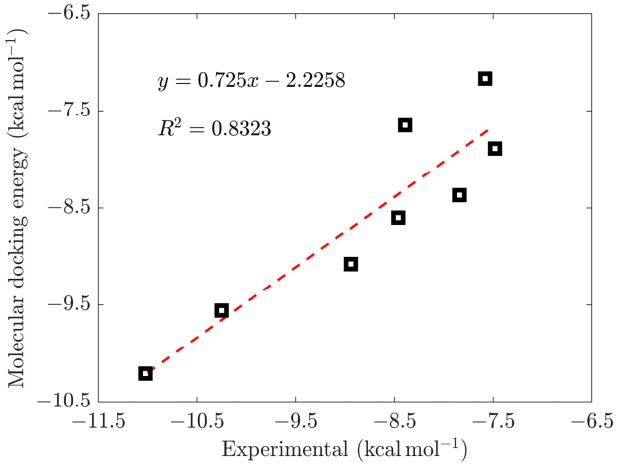


Figure 1. Docking protocol validation showing the relationship between the experimental data from the ITC and those calculated via molecular docking using AutoDock vina. The strong correlation value (R^2 = 0.83) between the experimental and molecular docking values justifies the reliability of the docking simulation used in the study.

Overall, the strong agreement between reproduced docking scores and experimentally reported values demonstrates the robustness and reproducibility of the employed docking protocol. These results support the suitability of the method for predicting binding affinities and accurately simulating ligand–receptor interactions in the present study.

3.2. Molecular Docking Interaction

In this study, 399 structurally analogous compounds to the reference drug Rifampicin were retrieved from SwissSimilarity and evaluated for their binding potential against *Mycobacterium tuberculosis* enoyl-acyl carrier protein reductase (*InhA*), a validated target for tuberculosis therapy. The active site for molecular docking was defined based on the cocrystallized structure of *InhA* in complex with the NH–NAD adduct, as reported by Marcio et al. (2007) [55]. Key residues within the binding pocket included PHE54, TYR43, ASP55, PHE64, GLU72, Val73, ILE74, TRP77, PHE117, CYS105, and TYR100. Molecular docking was performed using AutoDock Vina [35], and binding affinities were calculated to assess ligand-target interaction strength and stability (Table S1). Among the screened compounds, ZINC000013629834 displayed the most favourable binding energy (−10.90 kcal/mol), suggesting a higher affinity for the binding site than the native ligand (−9.38 kcal/mol). ZINC000253411694 and Rifampicin also exhibited strong binding affinities of −10.36 kcal/mol and −9.38 kcal/mol, respectively (see Table 1). The top two candidates, along with Rifampicin, were subsequently subjected to 100 ns molecular dynamics (MD) simulations to evaluate the stability and persistence of their interactions with *InhA* over time.

For ZINC000013629834, strong binding was primarily attributed to hydrogen bonds with GLY96, SER94, THR196 and ILE21, supported by van der Waals interactions involving PHE97, ILE16, MET147, LYS165, PHE149, MET199, ILE194, TYR158, PRO193, ILE22, GLY14, VAL65, GLN66, and ASP65. ZINC000253411694 formed hydrogen bonds with ILE21, THR196, and SER20, in addition to π–π stacking with PHE41, and van der Waals interactions with VAL73, PHE66, LYS65, PHE64, ARG60, and GLY71. Similarly, Rifampicin established hydrogen bonds with MET98, ILE21, and SER94, complemented by van der Waals contacts involving PHE97, THR196, GLY96, SER20, ALA22, MET147, LYS165, PHE149, TYR158, and GLY192 (see Table 2).

Table 2. Molecular interactions of selected ligands with the *InhA* active site and the distances in angstrom (Å) for conventional hydrogen bonds.

Compounds	Interactions with *InhA*	Distance for H Bonds (Å)
ZINC000013629834	Conventional Hydrogen Bond: GLY96, SER94, THR196, ILE21 Van der Waals: ASP64, GLN66, VAL65, GLY14, ALA22, PRO193, TYR158, ILE194, MET199, PHE149, LYS165, MET147, ILE16, PHE97 Carbon Hydrogen Bond: ILE95, SER20 Pi-Sigma: PHE41, ILE122	3.2, 1.8, 2.9 and 3.2
ZINC000253411694	Conventional Hydrogen Bond: ILE21, THR196, SER20 Carbon Hydrogen Bond: ASP64 Pi-Sigma: ILE95 Pi-Pi Stacked: PHE41 Pi-Alkyl: ILE16, ILE122, VAL65	3.2, 2.8 and 3.0
Rifampicin	Conventional Hydrogen Bond: MET98, SER94, ILE21 Van der Waals: ALA191, GLY192, TYR158, PHE149, LYS165, MET147, ALA22, SER20, GLY96, THR196, PHE97 Carbon Hydrogen Bond: ASP148, ILE194 Pi-Sigma: PRO193	3.1, 2.1 and 2.9

Across the three ligands, ILE21, SER20, and THR196 consistently engaged in hydrogen bonding, indicating their central role in ligand anchoring within the *InhA* active site. Additional residues such as SER94, GLY96, PHE97, and VAL65 frequently participated through hydrogen bonds or hydrophobic contacts, suggesting their importance in stabilizing inhibitor orientation (Figure 2). The recurrence of these interactions in chemically distinct ligands highlights them as potential pharmacophoric anchors for designing potent *InhA* inhibitors.

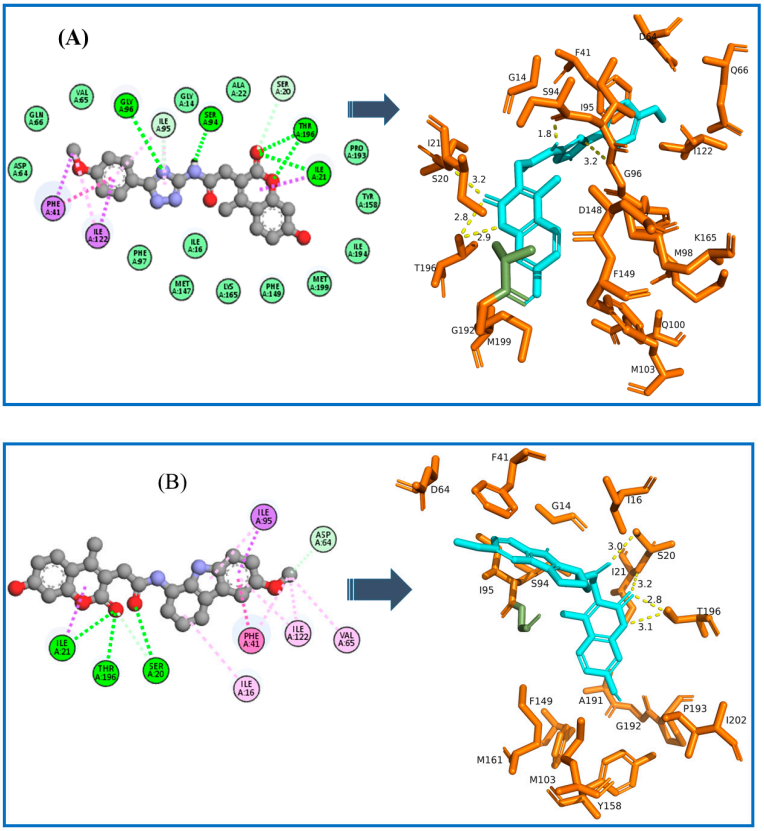


Figure 2. *Cont.*

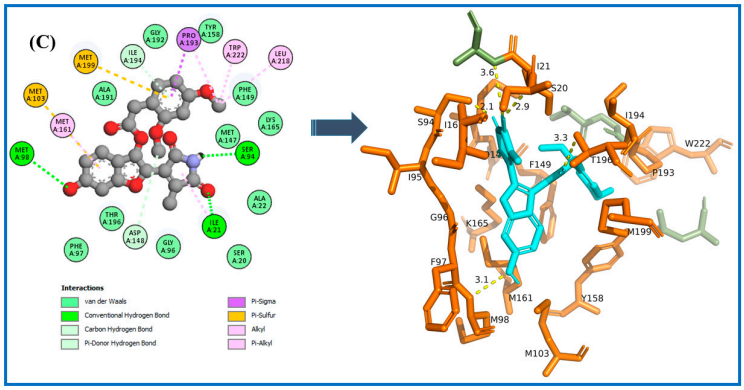


Figure 2. Interaction of residues from *InhA* with selected three compounds: (**A**) ZINC000013629834 (**B**) ZINC000253411694, and (**C**) Rifampicin.

3.3. Pharmacokinetic and Physicochemical Analysis

The physicochemical and pharmacokinetic profiles of ZINC000013629834, ZINC000253411694, and Rifampicin were evaluated in silico to assess their therapeutic potential. These parameters are essential for predicting the ability of a compound to reach its target site at concentrations sufficient to elicit a pharmacological effect. ADMET (absorption, distribution, metabolism, excretion, and toxicity) [56] was predicted using computational tools, providing a rapid and cost-effective alternative to experimental approaches. The assessment also included predictions of oral bioavailability and blood–brain barrier (BBB) permeability [57]. To enhance reliability, additional models such as the Brain or Intestinal EstimateD permeation method (BOILED-Egg) and Lipinski's Rule of Five (RO5) were applied via SwissADME. The pharmacokinetic and physicochemical properties of the three compounds are summarized in Table 3. ZINC000013629834 (MW = 406.39 g/mol; LogP = 1.81; HBD = 3; HBA = 7), ZINC000253411694 (MW = 432 g/mol; LogP = 3.08; HBD = 3; HBA = 5), and Rifampicin (MW = 437.4 g/mol; LogP = 2.46; HBD = 2; HBA = 8) all complied with Lipinski's Rule of Five, indicating favourable drug-likeness. All compounds exhibited LogP values below 5, within the optimal range (0.5–5.0) for drug-like molecules, reflecting balanced lipophilicity that supports membrane permeability while maintaining adequate aqueous solubility. This balance is consistent with effective absorption, distribution, and bioavailability and is generally associated with lower toxicity and improved interaction with hydrophobic targets.

Table 3. Physicochemical, pharmacokinetic, and medicinal chemistry descriptors of selected ligands.

Descriptor	ZINC000013629834	ZINC000253411694	Rifampicin
Total no. of atoms	30	32	32
Molecular weight (g/mol)	406.39	432.00	437.40
No. of H-bond acceptors	7	5	8
No. of H-bond donors	3	3	2
No. of rotatable bonds	6	5	7
TPSA (Å^2)	130.34	104.56	124.00
LogP	1.81	3.08	2.46
LogS (ESOL)	−7.37	−8.13	−6.76
GI absorbance	High	High	High
BBB permeant	No	No	No
LogKp (skin permeation) (cm/s)	−7.16	−6.74	−7.07

Table 3. *Cont.*

Descriptor	ZINC000013629834	ZINC000253411694	Rifampicin
Lipinski rule	0	0	0
Veber	0	0	0
Bioavailability score	0.55	0.55	0.55
Lead likeness	1	1	1
Synthetic accessibility	3.55	4.06	3.91

Notes: LogP = Logarithm of the partition coefficient; TPSA = Topological polar surface area, LogS = Aqueous solubility, GI = Gastrointestinal absorption, BBB = Blood–Brain Barrier.

All molecular weights were below 500 g/mol, supporting oral bioavailability, as higher values often reduce membrane permeability. The topological polar surface areas (TPSA= 124–130.34 Å^2) were below the recommended threshold of 140 Å^2, indicating favourable hydrogen bonding characteristics and supporting the ability of the compounds to cross cellular membranes, including the BBB, and to be absorbed via the gastrointestinal tract. None of the compounds violated Lipinski's rule, suggesting favourable overall physicochemical characteristics for oral administration.

Evaluation using Veber's rule [58], which is an oral drug-likeness guideline that predicts good oral bioavailability, has revealed zero violations, consistent with favourable conformational flexibility and polarity for oral bioavailability. The lead-likeness analysis indicated one physicochemical property violation, suggesting that although the compounds are promising drug candidates, structural optimization may be required to improve their lead profiles. Synthetic accessibility scores for ZINC000013629834, ZINC000253411694, and Rifampicin were 3.55, 4.06, and 3.91, respectively. These low-to-moderate values indicate that all three compounds can be synthesized using standard laboratory procedures without significant challenges.

3.4. Stability Analysis

3.4.1. Root Mean Squared Deviation

Root-mean squared deviation (RMSD) analysis was performed to evaluate the structural stability of the *InhA* protein and its ligand-bound complexes during molecular dynamics (MD) simulations. RMSD quantifies the average displacement of the C-α atoms at a given time point relative to their positions in the initial reference frame. Generally, low RMSD values indicate a stable protein or complex with minimal atomic displacement, whereas high RMSD values reflect increased structural fluctuations and potential instability [59,60].

In this study, the *InhA* protein was simulated in complex with the top three ligands—ZINC000013629834, ZINC000253411694, and Rifampicin—selected based on their highest binding affinities from molecular docking. The RMSD values for these complexes were 0.16792 ± 0.01290 nm, 0.17485 ± 0.00254 nm, and 0.29655 ± 0.01620 nm for ZINC000013629834, ZINC000253411694, and Rifampicin, respectively. All values were below the commonly accepted threshold of 2 Å (~0.2 nm), indicating stable complex formation throughout the 100 ns simulations (Figure 3a).

The RMSD probability distribution plots revealed a single dominant peak for all systems (Figure 3b), consistent with the time-resolved RMSD profiles (Figure 3a). The trajectories exhibited transient fluctuations during the first 20 ns, followed by stabilization between 20–40 ns and again from 70–100 ns, suggesting an initial structural adaptation phase before reaching equilibrium. These observations indicate that all three ligands maintained stable binding within the *InhA* active site during the simulation period.

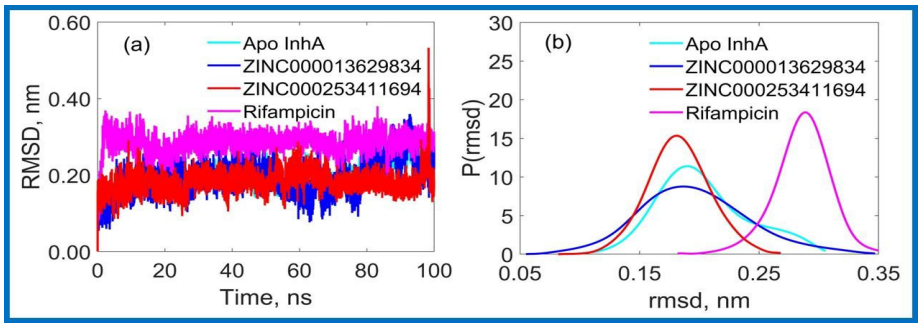


Figure 3. Root Mean Square Deviation of *InhA*, and when complexed with ZINC000013629834, ZINC000253411694, Rifampicin interacting with Amino Acids from *InhA* (**a**) time-dependent and (**b**) probability density of RMSD.

Moreover, MD simulations provided additional insight beyond molecular docking by allowing conformational flexibility of both the protein and ligands over time. Key protein–ligand interactions were monitored at 0 ns, 50 ns, and 100 ns, focusing particularly on hydrogen bond formation in the ZINC000013629834 complex. The hydrogen bond distance decreased from 2.412 Å at the beginning to 1.780 Å at 50 ns, and further to 0.971 Å at 100 ns (Figure 3), indicating strengthened interactions and dynamic rearrangements of key binding site residues during the simulation.

3.4.2. Solvent Accessible Surface Area (SASA)

Another key parameter evaluated after the MD simulations was the Solvent Accessible Surface Area (SASA), which provides insights into the conformational dynamics of the protein–ligand complex, reflecting ligand binding effects and overall complex stability. In general, a decrease in SASA indicates structural compaction and burial of hydrophobic regions, whereas an increase suggests unfolding or exposure of previously buried residues [61–63]. In this study, SASA was calculated for *InhA* complexed with ZINC000013629834, ZINC000253411694, and Rifampicin, yielding average values of 145 nm^2, 143 nm^2, and 142 nm^2, respectively (Figure 4a,b) for time dependence and probability of SASA respectively. The relatively stable SASA values over the 100 ns simulation period indicate that the complexes remained conformationally stable, supporting the potential therapeutic relevance of the identified compounds.

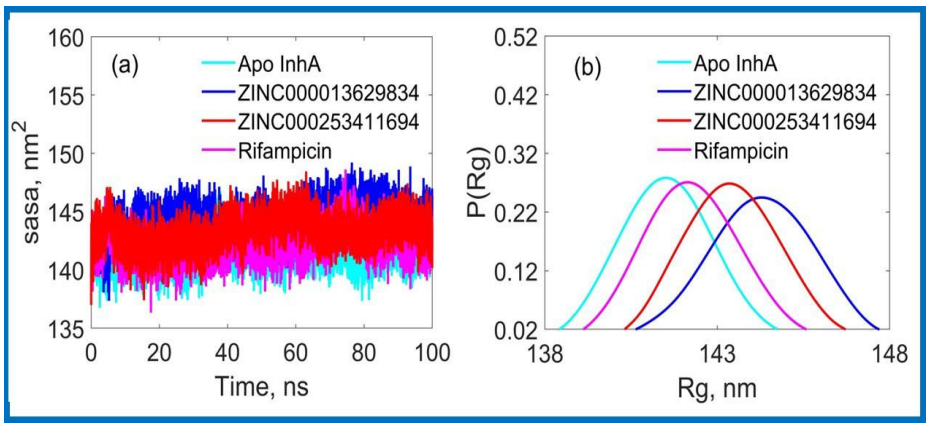


Figure 4. Solvent Accessible Surface Area of *InhA*, and when complexed with ZINC000013629834, ZINC000253411694, and Rifampicin. (**a**) Time-dependent and (**b**) probability density of RMSD.

3.4.3. Radius of Gyration (Rg)

The radius of gyration (R_g) was analyzed as an additional parameter to evaluate the conformational stability of the protein during the simulations. This parameter represents the mass-weighted root mean square distance of the protein atoms from their common centre of mass [64], and it serves as a measure of the overall compactness of the protein–ligand complex over time. Typically, a lower or decreasing R_g value reflects structural compaction and stable folding, whereas higher or fluctuating values suggest conformational instability and unfolding.

In this study, R_g was computed for the *InhA* complexes with ZINC000013629834, ZINC000253411694, and Rifampicin. The average R_g values of all three complexes were approximately 1.83 nm. For ZINC000013629834, R_g stabilized at 1.80 nm during the first 30 ns, increased slightly to 1.84 nm by 50 ns, and remained stable up to 100 ns. A similar trend was observed for ZINC000253411694. In the Rifampicin complex, R_g started at 1.85 nm, gradually decreased to 1.80 nm by 30 ns, and fluctuated moderately around 1.82 nm for the remainder of the trajectory Figure 5a for time-dependent plots and Figure 5b for probability distributions). Despite these minor variations, the protein retained a compact conformation throughout the 100 ns simulations. The relatively stable R_g values across all ligand-bound systems suggest enhanced conformational stability, most likely due to strong and persistent protein–ligand interactions.

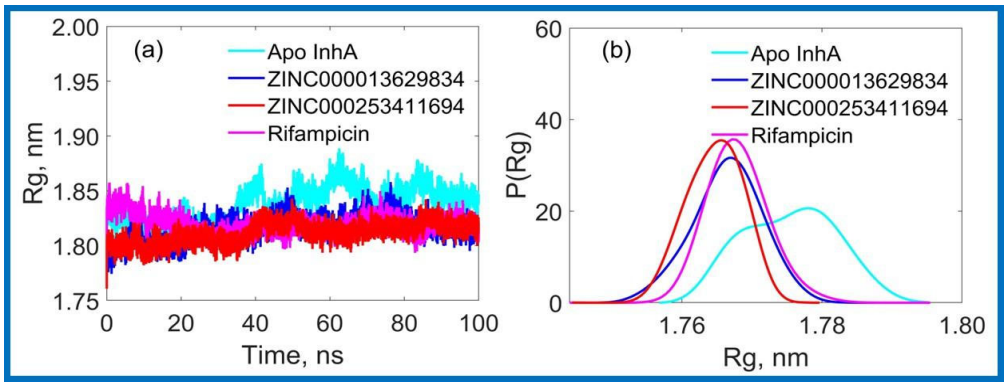


Figure 5. Radius of gyration for *InhA*, and when complexed with ZINC000013629834, ZINC000253411694, Rifampicin (**a**) time dependent and (**b**) probability density of R_g.

3.4.4. Root Mean Squared Fluctuations (RMSF)

To gain deeper insights into the conformational stability and structural flexibility of residues within each protein–ligand system, root mean square fluctuation (RMSF) analyses were performed over the 100 ns MD trajectories [65]. RMSF provides residue-wise information on atomic positional deviations, allowing the identification of flexible loops, binding site rearrangements, and regions of structural stabilization upon lig- and binding. As illustrated in Figure 6, the *InhA* protein complexed with ZINC000013629834, ZINC000253411694, and Rifampicin displayed broadly similar fluctuation profiles, reflecting comparable overall stability across the three systems. In the ZINC000013629834 complex, distinct fluctuations were observed around residues 48–52, 153, and 210–222, with the most pronounced peak occurring at residue 210, where the fluctuation reached approximately 0.3 nm. A similar trend was observed in the ZINC000253411694 complex, though with slightly lower amplitudes, suggesting reduced flexibility in those regions. In contrast, the Rifampicin complex showed a more noticeable degree of residue fluctuation, particularly in the loop regions, which exhibited higher mobility compared to the novel ligand complexes. These observations indicate that while all three ligands preserved the structural integrity of *InhA*, ZINC000013629834 and ZINC000253411694 promoted relatively greater conformational

stability compared to Rifampicin. The reduced flexibility in the novel ligand complexes highlights their ability to stabilize key structural elements of the protein, reinforcing their potential as promising therapeutic candidates.

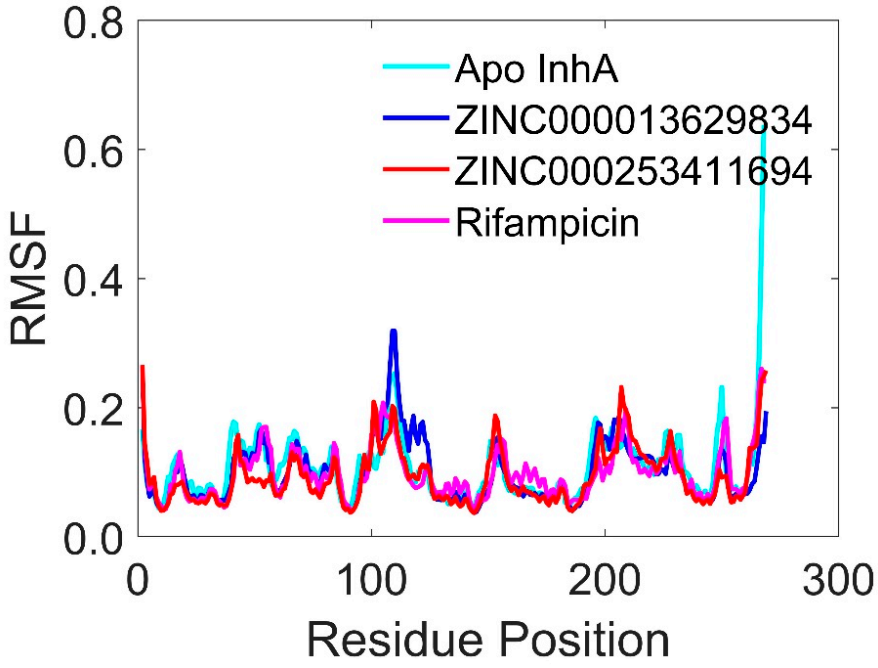


Figure 6. Root Mean Square Fluctuation for *InhA*, and when complexed with ZINC000013629834, ZINC000253411694 and Rifampicin.

3.5. Hydrogen Bond Analysis

The determination of the intermolecular hydrogen bond is crucial for identifying the key contributors to protein–ligand interactions [66,67]. Monitoring the number and persistence of hydrogen bonds during molecular dynamics (MD) simulations provides valuable information on the stability and strength of the complexes [68]. In this study, the hydrogen bonds between *InhA* and the selected ligands were analyzed over a 100 ns MD trajectory. Throughout the simulations, dynamic hydrogen bond networks were observed, with fluctuations ranging between one and six bonds (Figure 7). For the *InhA*–ZINC000013629834 complex, strong interactions ranging from one to five hydrogen bonds were recorded, with predominant occupancies at two, three and four bonds. These interactions were primarily stabilized by residues GLY96, SER94, THR196, and ILE21 with distances of 3.2, 1.8, 2.9 and 3.2 Å respectively see Table 2. Similarly, the *InhA*–ZINC000253411694 complex exhibited a range of zero to five hydrogen bonds, most frequently maintaining two, three, or four bonds (Figure 8). The key residues involved were ILE21, THR196, and SER20 with distances of 3.2, 2.8 and 3.0 Å, respectively (Table 2) which were also identified during the docking simulations. In comparison, the reference inhibitor Rifampicin formed the most stable hydrogen bonding network with *InhA*, fluctuating between two and six bonds (Figure 9). The predominant interactions, maintained at three, four, and five bonds, involved MET98, SER94, and ILE21 with distances of 3.1, 2.1 and 2.9 Å, respectively. The persistence of these hydrogen bonds across the trajectories highlights their role in stabilizing the protein-ligand complexes, suggesting that stability is influenced not only by the size of the compounds but also by the nature of their functional groups [69].

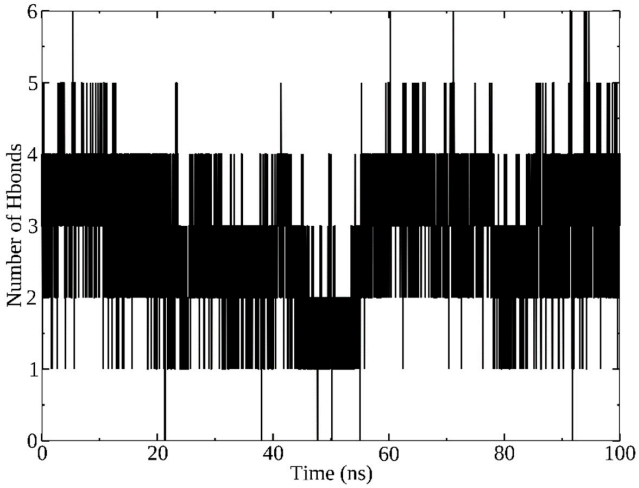


Figure 7. Hydrogen analysis for *InhA* complexed with ZINC000013629834.

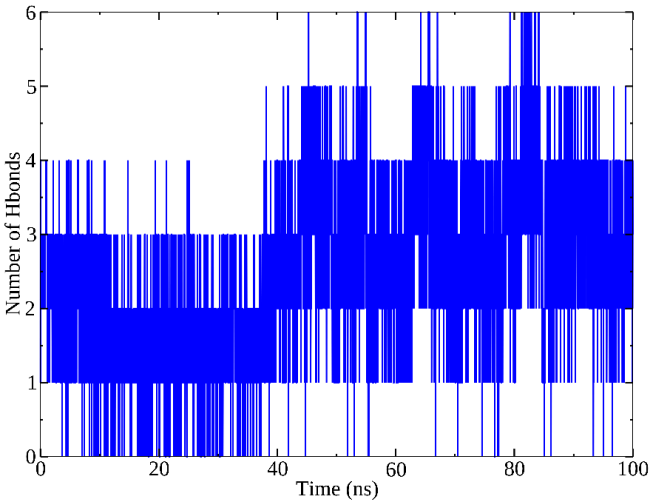


Figure 8. Hydrogen analysis for *InhA* complexed with ZINC000253411694.

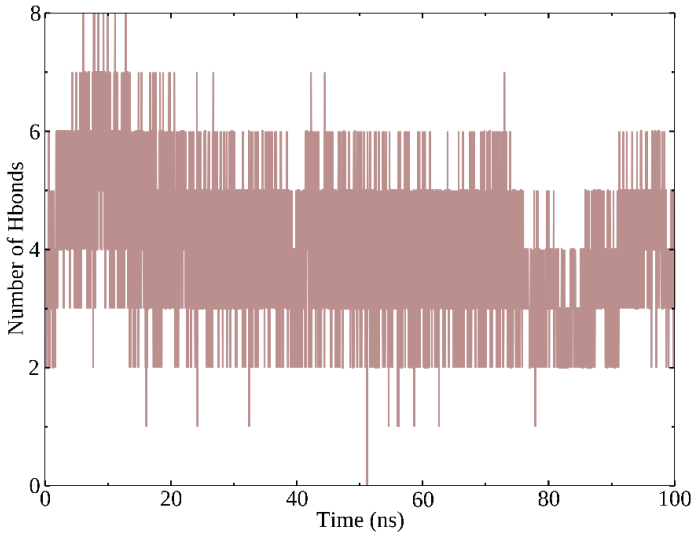


Figure 9. Hydrogen analysis for *InhA* complexed with Rifampicin.

3.6. Free Energy Landscape Analysis

The free energy landscape (FEL) analysis provides crucial insights into the stability of apo protein and protein–ligand complexes, particularly in the prediction of binding

transition states and metastable conformations, which are of significant importance in drug design [70]. In this study, the Gibbs free energy landscapes of the systems were computed within an energy range of 0 to 14 kcal/mol. FELs were derived using the Boltzmann distribution equation; see Equation (5).

$$\Delta G = -RT \ln P \tag{5}$$

where G represents the probability of a given conformation along the reaction coordinates, and PC1 and PC2 denote the first and second principal components, respectively, R is molar gas constant and T is the absolute temperature. These parameters capture the dominant conformational variations in the protein and its complexes. The conformational stability of the protein–ligand complexes was further assessed using two-dimensional free energy landscape (FEL) plots constructed from the principal components PC1 and PC2 obtained through PCA (as defined in Equation (5)). In the FEL maps, deep blue regions represent global minima corresponding to low free-energy, highly stable conformational states, whereas yellow regions denote higher-energy, less stable conformations. This visualization provides an intuitive summary of the dominant motions captured by the first two principal components and highlights the preferred conformational basins sampled during the simulation. The FEL analysis revealed distinct stability patterns across the systems. The apo *InhA* protein exhibited one major global minimum surrounded by two local minima (Figure 10). The *InhA*–ZINC000013629834 complex displayed multiple metastable states with well-defined global minima, suggesting conformational transitions represented by three discrete basins separated by energy barriers (Figure 11). For the *InhA*–ZINC000253411694 complex, one dominant global minimum and two additional metastable conformations were observed (Figure 12). The *InhA*–Rifampicin complex exhibited two major global minima with several local minima (Figure 13).

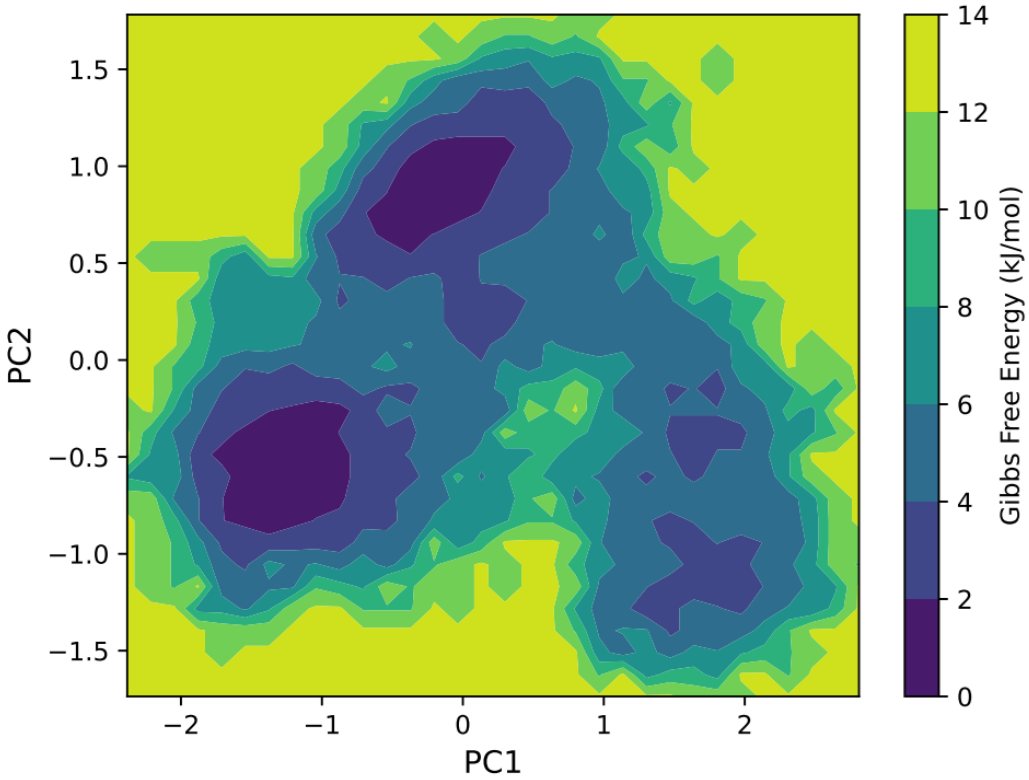


Figure 10. 2D free energy landscape for Apo protein *InhA*.

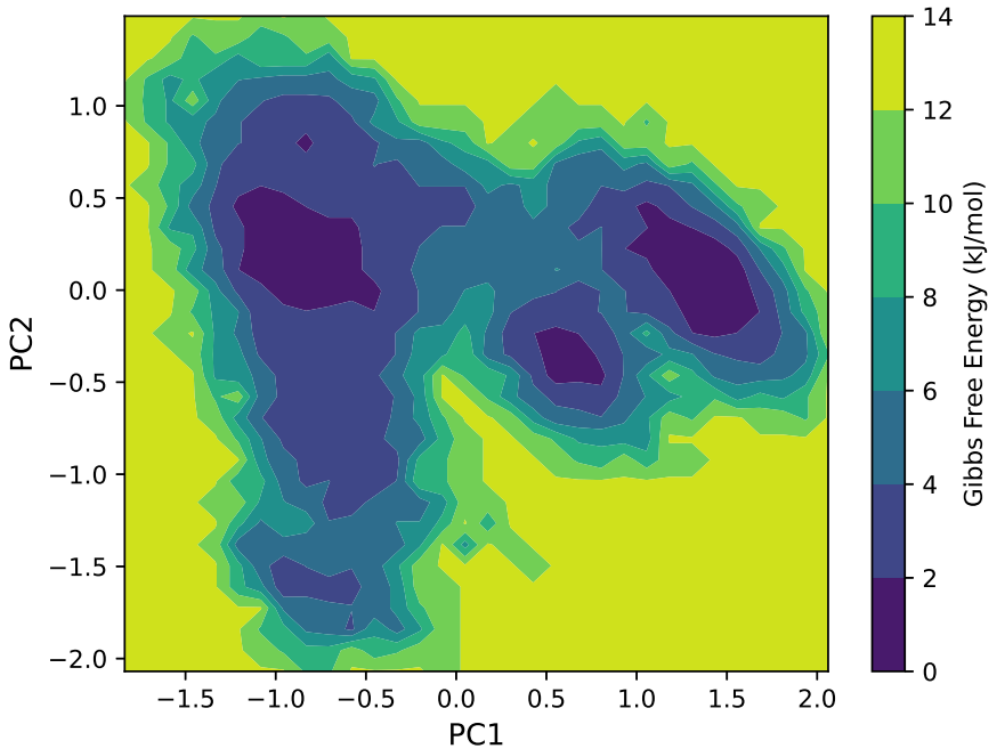


Figure 11. 2D free energy landscape for the complex for the Ligand ZINC000013629834.

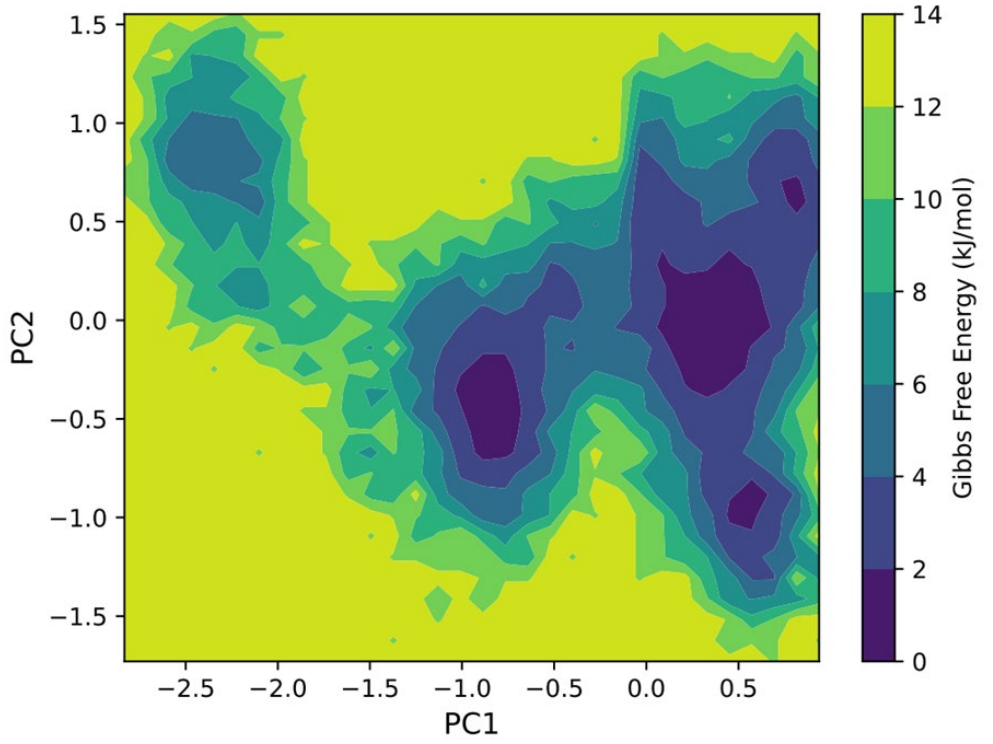


Figure 12. 2D free energy landscape for the complex for the Ligand ZINC000253411694.

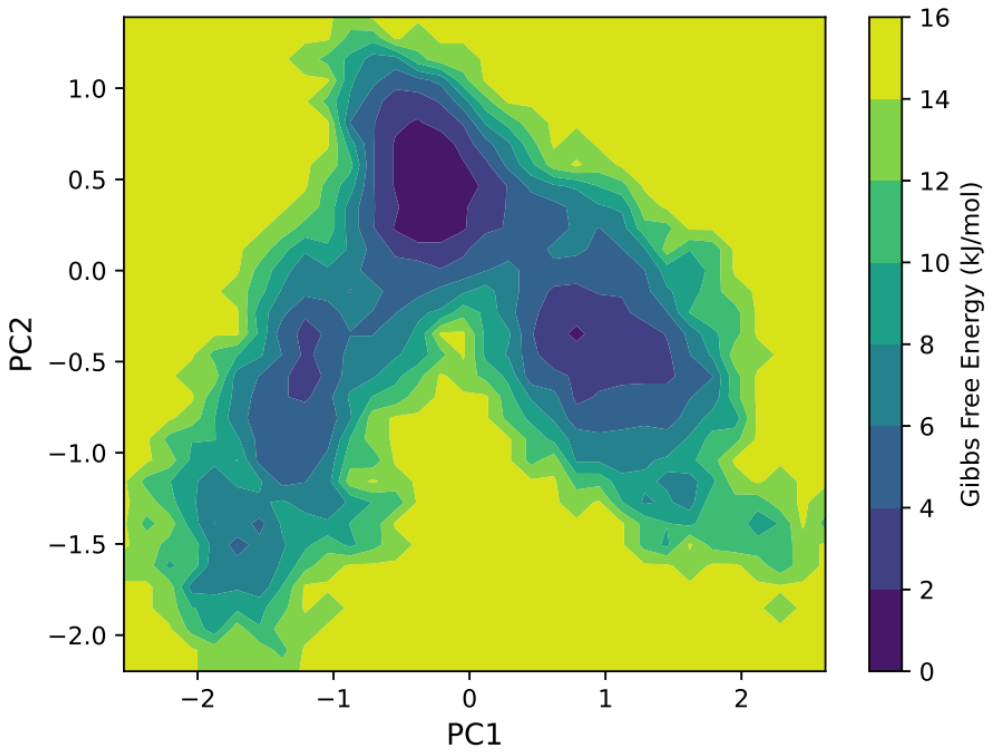


Figure 13. 2D free energy landscape for the complex of the Ligand Rifampicin.

Overall, these FEL results demonstrate that *InhA* and its ligand-bound complexes adopt stable conformational states, supporting the potential inhibitory properties of the identified compounds.

3.7. MM/PBSA Binding–Free Energy Analysis

To further validate the docking results and quantify the binding affinities of the protein–ligand complexes, we performed molecular mechanics Poisson–Boltzmann surface area (MM/PBSA) analysis. This approach estimates the binding free energy by decomposing the total energy into contributions from van der Waals, electrostatic, polar solvation, nonpolar solvation, and overall energy. The calculated binding free energies are summarized in Table 4.

Table 4. Binding energy calculations of ZINC000013629834, ZINC000253411694 and Rifampicin in kJ/mol.

Complexes	ΔEvdW	ΔE_{elect}	ΔG_{PB}	ΔG_{SASA}	$\Delta G_{binding}$
ZINC000013629834	−201.951 ± 0.974	−67.275 ± 0.913	200.601 ± 1.300	−21.560 ± 0.095	−90.159 ± 1.499
ZINC000253411694	−185.814 ± 1.215	−67.608 ± 0.878	183.415 ± 1.231	−21.557 ± 0.114	−91.646 ± 1.524
Rifampicin	−216.680 ± 1.366	−90.289 ± 1.775	239.704 ± 1.340	−23.364 ± 0.092	−90.734 ± 1.431

Among the studied complexes ZINC000013629834, ZINC000253411694, and Rifampicin, the binding affinity of ZINC000013629834 was primarily stabilized by van der Waals interactions (−201.951 kJ/mol), complemented by electrostatic interactions (−67.275 kJ/mol) and nonpolar solvation energy (−21.56 kJ/mol), whereas polar solvation opposed binding (+200.601 kJ/mol) see Figure 14a. The total binding free energy for this complex was −91.159 kJ/mol. For ZINC000253411694, the energy decomposition followed a similar pattern, with van der Waals contributions of −185.814 kJ/mol, electrostatic interactions of −67.608 kJ/mol, and polar solvation opposing binding at 183.415 kJ/mol,

resulting in an overall binding free energy of −91.646 kJ/mol is the most favourable among the studied complexes see Figure 14b. Rifampicin, used as a reference compound, exhibited higher van der Waals (−216.680 kJ/mol) and electrostatic (−90.289 kJ/mol) contributions than the two ZINC compounds. However, these were counterbalanced by a larger polar solvation energy of +239.704 kJ/mol, yielding a total binding free energy of −90.734 kJ/mol, comparable to the other complexes as presented at Figure 14c.

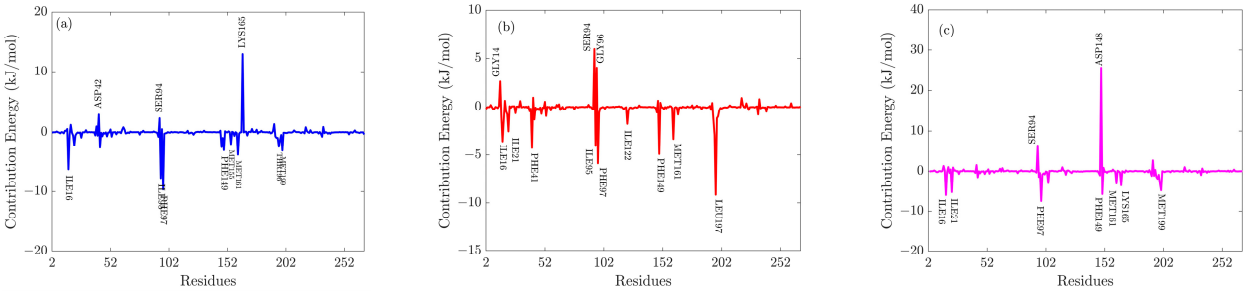


Figure 14. The energy contribution to protein-ligand binding (**a**) ZINC000013629834, (**b**) ZINC000253411694 and (**c**) Rifampicin.

The observed differences in the energy contributions of the complexes motivated a detailed per-residue decomposition analysis in order to identify key amino acids involved in protein–ligand stabilization. For the ZINC000013629834 complex, the most favourable contributions were provided by PHE97 (−9.66 kJ/mol), ILE95 (−7.74 kJ/mol), ILE16 (−6.25 kJ/mol), MET161 (−3.80 kJ/mol), and PHE149 (−3.04 kJ/mol). In contrast, ASP42 (+2.94 kJ/mol), SER94 (+2.33 kJ/mol), and LYS165 (+12.96 kJ/mol) exhibited unfavourable contributions, suggesting local steric or electrostatic repulsion. In the ZINC000253411694 complex, stabilizing residues included LEU197 (−9.16 kJ/mol), PHE97 (−5.88 kJ/mol), ILE95 (−4.05 kJ/mol), PHE41 (−4.26 kJ/mol), and MET161 (−3.33 kJ/mol). Conversely, unfavourable contributions arose from SER94 (+5.95 kJ/mol), GLY96 (+4.02 kJ/mol), and GLU219 (+0.92 kJ/mol). For the Rifampicin complex, the key stabilizing residues were PHE97 (−7.48 kJ/mol), ILE21 (−5.26 kJ/mol), ILE16 (−5.99 kJ/mol), ARG43 (−1.55 kJ/mol), and MET103 (−2.99 kJ/mol). The main destabilizing residues were SER94 (+6.36 kJ/mol), ASP42 (+1.50 kJ/mol), and ASP115 (+0.95 kJ/mol).

Taken together, these findings confirm that drug stabilization within the binding pocket is primarily influenced by conserved hydrophobic residues, particularly PHE97, ILE95/21, and MET161/103, which consistently provided favourable contributions across all three complexes. In contrast, SER94 and ASP42 were repeatedly associated with unfavourable interactions, indicating that this region of the binding site is energetically unsuitable for ligand accommodation. Overall, the results highlight the presence of conserved energetic hotspots that support common interaction mechanisms. At the same time, variations in residue-specific contributions help explain the observed differences in binding affinities among the complexes. In general, the MM/PBSA analysis indicates that ZINC000253411694 exhibited the strongest binding affinity (−91.646 kJ/mol), followed closely by Rifampicin (−90.734 kJ/mol) and ZINC000013629834 (−91.159 kJ/mol). These results confirm that the selected drug candidates exhibited slightly stronger binding affinities compared to the reference Rifampicin.

It is important to note that the docking scores (kcal/mol) and MM/PBSA free energies (kJ/mol) are reported in their native units as produced by AutoDock Vina and g_mmpbsa, respectively.

4. Discussion

The persistence of tuberculosis (TB) is largely attributed to mutations in the *rpoB* gene, which confer resistance to first-line drugs such as Rifampicin and present a major barrier to effective TB management. Rifampicin exerts its therapeutic activity by inhibiting RNA polymerase; however, resistance mutations allow bacterial survival without compromising viability, thereby limiting the long-term utility of this frontline drug. Designing Rifampicin analogues that engage alternative mechanisms of action, such as inhibition of enoyl-acyl carrier protein reductase (*InhA*), offers a rational strategy to overcome rpoB-mediated resistance. In this study, two Rifampicin analogues—ZINC000013629834 and ZINC000253411694—were identified as promising candidates, showing stronger binding affinities toward *InhA* compared to Rifampicin. All three complexes engaged conserved residues (ILE21, SER20, THR196, PHE97, and ILE95) that are crucial for ligand stabilization and inhibition at the *InhA* binding site. These findings are consistent with previous crystallographic and computational studies highlighting the importance of hydrophobic and hydrogen-bonding interactions at these residues in stabilizing *InhA*–inhibitor complexes.

Importantly, ADMET profiling demonstrated that both analogues satisfied Lipinski's Rule of Five, exhibited high predicted gastrointestinal absorption, and showed no major toxicity alerts, highlighting their favourable pharmacokinetic properties. This aligns with earlier reports where Rifampicin derivatives optimized for drug-likeness displayed improved oral bioavailability and reduced toxicity. Molecular dynamics simulations confirmed the stability of the protein–ligand complexes, with reduced conformational fluctuations reflected in RMSD values of 0.16792 nm, 0.17485 nm, and 0.29655 nm for ZINC000013629834, ZINC000253411694, and Rifampicin, respectively. Notably, the analogues maintained RMSD values below 0.2 nm, suggesting stronger structural stability compared to Rifampicin. Similar trends have been observed in MD simulations of *InhA* inhibitors, where stable RMSD trajectories correlate with higher inhibitory potency.

Furthermore, MM/PBSA binding free energy calculations revealed comparable affinities, with ZINC000253411694 (−91.65 kJ/mol), ZINC000013629834 (−90.16 kJ/mol), and Rifampicin (−90.73 kJ/mol). These values are consistent with prior computational analyses of *InhA*–ligand complexes, which reported binding free energies in a similar range for clinically relevant inhibitors. Collectively, these findings indicate that optimized Rifampicin analogues targeting *InhA* may overcome rpoB-associated resistance and represent promising lead compounds for next-generation anti-TB drug development. By aligning with structural and simulation-based evidence from previous studies, this work further underscores the feasibility of rationally designing Rifampicin analogues to broaden therapeutic strategies against drug-resistant TB.

The results obtained through docking, ADMET profiling, MD simulations, and MM/PBSA calculations provide strong computational evidence that the two analogues possess the characteristics of potential *InhA* inhibitors. However, these findings should be viewed as preliminary until validated experimentally. Future studies should incorporate biochemical inhibition assays and biophysical binding measurements to confirm the predicted activity and further optimize these compounds.

In addition, future studies should evaluate the in vitro antibacterial activity of the top analogues against *Mycobacterium tuberculosis* H37Rv and Rifampicin-resistant strains to confirm that the predicted *InhA* inhibition translates into whole cell efficacy.

Although this work focuses on *InhA*, a comprehensive off-target assessment is important in drug development. Because this study represents early-stage computational screening, detailed pathogen or human selectivity profiling was beyond its scope. However, ADMET predictions from pkCSM and SwissADME provided preliminary insights into

potential off-target and safety risks. Broader off-target evaluation should be pursued in future studies as the identified analogues advance toward experimental validation.

5. Conclusions

This study demonstrates that Rifampicin analogues can be rationally redesigned to target *InhA* and overcome RpoB-mediated resistance. Among the screened compounds, ZINC000253411694 and ZINC000013629834 exhibited potent inhibition, stable interactions, and superior pharmacokinetic profiles compared to Rifampicin. These findings highlight the use of analogue-based design as a promising strategy to extend rifamycin efficacy and tackle drug resistance, addressing the urgent need for novel approaches in the post-antibiotic era. Although the present work is computational, the identified analogues exhibit promising pharmacokinetic, structural, and energetic properties that warrant advancement to experimental validation. Future work will include enzyme inhibition assays and biophysical binding studies to confirm the predicted *InhA* inhibitory activity and evaluate their potential as next-generation anti-TB agents.

Supplementary Materials: The following supporting information can be downloaded at: https://www.mdpi.com/article/10.3390/chemengineering10020028/s1, Figure S1: Docking and Re-docking results used as a reference from the study by [54]; Table S1: Summary of binding energy reproduced from experimental binding energy by molecular docking; Table S2: Comparison of the docking and re-docking score (kcal/mol) with acetylcholinesterase (PDBID: 3LII) results used from a study as reference from [54].

Author Contributions: Conceptualization, L.P., methodology L.P. and A.S.P.; validation L.P. and formal analysis, L.P. and A.S.P.; data curation, L.P. All authors have read and agreed to the published version of the manuscript.

Funding: This research received no external funding.

Data Availability Statement: Data will be provided by Lucas Paul (E-mail: lucas.paul@udsm.ac.tz, lucaspaul33@gmail.com) upon reasonable request.

Acknowledgments: The authors are grateful to the DUCE Chemistry computational unit for support of computational facilities.

Conflicts of Interest: The authors declare no conflicts of interest.

References

1. Mohammadnabi, N.; Shamseddin, J.; Emadi, M.; Bodaghi, A.B.; Varseh, M.; Shariati, A.; Rezaei, M.; Dastranj, M.; Farahani, A. Mycobacterium tuberculosis: The mechanism of pathogenicity, immune responses, and diagnostic challenges. *J. Clin. Lab. Anal.* **2024**, *38*, e25122. [CrossRef] [PubMed]
2. Black, R.E.; Perin, J.; Yeung, D.; Rajeev, T.; Miller, J.; Elwood, S.E.; Platts-Mills, J.A. Estimated global and regional causes of deaths from diarrhoea in children younger than 5 years during 2000–21: A systematic review and Bayesian multinomial analysis. *Lancet Glob. Health* **2024**, *12*, e919–e928. [CrossRef] [PubMed]
3. Çelik, M.; Döker, M.F.; Kırlangıçoğlu, C.; Ünsal, Ö.; Gökçeoğlu, S.; Ceylan, M.R.; Karabay, O. Comprehensive spatial investigation of tuberculosis dynamics and affecting factors in Şanlıurfa, Türkiye (2016–2023). *GeoHealth* **2025**, *9*, e2024GH001235. [CrossRef] [PubMed]
4. Chen, Z.; Wang, T.; Du, J.; Sun, L.; Wang, G.; Ni, R.; An, Y.; Fan, X.; Li, Y.; Guo, R.; et al. Decoding the WHO Global Tuberculosis Report 2024: A critical analysis of global and Chinese key data. *Zoonoses* **2025**, *5*, 999. [CrossRef]
5. Katende-Kyenda, L.N. Determinants of non-adherence to anti-tuberculosis treatment in a public primary healthcare clinic in South Africa: Improving the quality of long-term care. *Int. J. Environ. Res. Public Health* **2025**, *22*, 1209. [CrossRef]
6. Olivier, C.; Luies, L. WHO goals and beyond: Managing HIV/TB co-infection in South Africa. *SN Compr. Clin. Med.* **2023**, *5*, 251. [CrossRef]
7. Brode, S.K.; Dwilow, R.; Kunimoto, D.; Menzies, D.; Khan, F.A. Drug-resistant tuberculosis. *Can. J. Respir. Crit. Care Sleep Med.* **2022**, *6*, 109–128. [CrossRef]

8. Chopra, H.; Mohanta, Y.K.; Rauta, P.R.; Ahmed, R.; Mahanta, S.; Mishra, P.K.; Panda, P.; Rabaan, A.A.; Alshehri, A.A.; Othman, B.; et al. Advances in nanotechnology-based therapeutics, drug delivery, diagnostics and vaccines: Multidimensional applications in tuberculosis disease management. *Pharmaceuticals* **2023**, *16*, 581. [CrossRef]
9. Islam, M.N.; Mili, M.A.; Jahan, I.; Chakma, C.; Munalisa, R. Immunological and neurological signatures of the co-infection of HIV and HTLV: Current insights and future perspectives. *Viruses* **2025**, *17*, 545. [CrossRef]
10. Abdul-Ghani, R.; Al-Awadi, A.; Al-Aghbari, N.; Al-Mikhlafy, A.A.; Abdulmoghni, S.S.; Al-Dobai, S.S.; Nauman, N.F. Latent tuberculosis infection and diagnostic performance of the tuberculin skin test among type 2 diabetics in Sana'a city, Yemen. *BMC Infect. Dis.* **2024**, *24*, 1005. [CrossRef]
11. Chen, Q.; Ren, N.; Liu, S.; Qian, Z.; Li, M.; Mustapha, A.; Luo, W.; Li, J.; Wang, W.; Hao, C. Prevalence of tuberculosis among migrants under national screening programs: A systematic review and meta-analysis. *Glob. Health Res. Policy* **2025**, *10*, 24. [CrossRef] [PubMed]
12. Lange, C.; Dheda, K.; Chesov, D.; Mandalakas, A.M.; Udwadia, Z.; Horsburgh, C.R. Management of drug-resistant tuberculosis. *Lancet* **2019**, *394*, 953–966. [CrossRef]
13. Zein-Eddine, R.; Ramuz, M.; Refrégier, G.; Lutzeyer, J.F.; Aleksandrov, A.; Myllykallio, H. Key challenges in tuberculosis drug discovery: What does the future hold? *Expert Opin. Drug Discov.* **2025**, *20*, 1115–1130. [CrossRef]
14. Tiberi, S.; Utjesanovic, N.; Galvin, J.; Centis, R.; D'AMbrosio, L.; Boom, M.v.D.; Zumla, A.; Migliori, G.B. Drug-resistant TB: Latest developments in epidemiology, diagnostics and management. *Int. J. Infect. Dis.* **2022**, *124*, S20–S25. [CrossRef] [PubMed]
15. Patra, J.; Irving, H.; Maini, P.; Liang, J.; Patra, A.; Paradkar, M.; Rehm, J. Treatment outcomes among children and adolescents with XDR and pre-XDR tuberculosis: A systematic review and meta-analysis. *PLoS Glob. Public Health* **2025**, *5*, e0003754. [CrossRef]
16. Wallis, R.S.; Kim, P.; Cole, S.; Hanna, D.; Andrade, B.B.; Maeurer, M.; Schito, M.; Zumla, A. Tuberculosis biomarker discovery: Developments, needs, and challenges. *Lancet Infect. Dis.* **2013**, *13*, 362–372. [CrossRef]
17. Abdallah, E.M.; Alhatlani, B.Y.; Menezes, R.d.P.; Martins, C.H.G. Back to nature: Medicinal plants as promising sources for antibacterial drugs in the post-antibiotic era. *Plants* **2023**, *12*, 3077. [CrossRef]
18. Newman, D.J.; Cragg, G.M. Natural products as sources of new drugs over the last 25 years. *J. Nat. Prod.* **2007**, *70*, 461–477. [CrossRef]
19. Gangwal, A.; Lavecchia, A. Artificial intelligence in natural product drug discovery: Current applications and future perspectives. *J. Med. Chem.* **2025**, *68*, 3948–3969. [CrossRef]
20. Neumann, A.; Marrison, L.; Klein, R. Relevance of the trillion-sized chemical space "eXplore" as a source for drug discovery. *ACS Med. Chem. Lett.* **2023**, *14*, 466–472. [CrossRef]
21. Daina, A.; Michielin, O.; Zoete, V. SwissADME: A web tool to evaluate pharmacokinetics, drug-likeness and medicinal chemistry friendliness of small molecules. *Sci. Rep.* **2017**, *7*, 42717. [CrossRef] [PubMed]
22. Gelpi, J.; Hospital, A.; Goñi, R.; Orozco, M. Molecular dynamics simulations: Advances and applications. *Adv. Appl. Bioinform. Chem.* **2015**, *8*, 37–47. [CrossRef] [PubMed]
23. Sliwoski, G.; Kothiwale, S.; Meiler, J.; Lowe, E.W. Computational methods in drug discovery. *Pharmacol. Rev.* **2014**, *66*, 334–395. [CrossRef] [PubMed]
24. Rose, P.W. The RCSB Protein Data Bank: Integrative view of protein, gene and 3D structural information. *Nucleic Acids Res.* **2016**, *45*, D271–D281. [CrossRef]
25. Morris, G.M.; Huey, R.; Lindstrom, W.; Sanner, M.F.; Belew, R.K.; Goodsell, D.S.; Olson, A.J. AutoDock4 and AutoDockTools4: Automated docking with selective receptor flexibility. *J. Comput. Chem.* **2009**, *30*, 2785–2791. [CrossRef]
26. Pettersen, E.F.; Goddard, T.D.; Huang, C.C.; Meng, E.C.; Couch, G.S.; Croll, T.I.; Morris, J.H.; Ferrin, T.E. ChimeraX: Structure visualization for researchers, educators, and developers. *Protein Sci.* **2021**, *30*, 70–82. [CrossRef]
27. Bragina, M.E.; Daina, A.; Perez, M.A.S.; Michielin, O.; Zoete, V. SwissSimilarity 2021: Novel chemical libraries and additional methods for ligand-based virtual screening. *Int. J. Mol. Sci.* **2022**, *23*, 811. [CrossRef]
28. O'Boyle, N.M.; Banck, M.; James, C.A.; Morley, C.; Vandermeersch, T.; Hutchison, G.R. Open Babel: An open chemical toolbox. *J. Cheminform.* **2011**, *3*, 33. [CrossRef]
29. Halgren, T.A. Merck molecular force field. I. Basis, form, scope, parameterization, and performance of MMFF94. *J. Comput. Chem.* **1996**, *17*, 490–519. [CrossRef]
30. Lim, V.T.; Hahn, D.F.; Tresadern, G.; Bayly, C.I.; Mobley, D.L. Benchmark assessment of molecular geometries and energies from small molecule force fields. *F1000Research* **2020**, *9*, 1390. [CrossRef]
31. Lipinski, C.A.; Lombardo, F.; Dominy, B.W.; Feeney, P.J. Experimental and computational approaches to estimate solubility and permeability in drug discovery and development settings. *Adv. Drug Deliv. Rev.* **1997**, *23*, 3–25. [CrossRef]
32. Abdullahi, S.H.; Moin, A.T.; Uzairu, A.; Umar, A.B.; Ibrahim, M.T.; Usman, M.T.; Nawal, N.; Bayil, I.; Zubair, T. Molecular docking and MD simulation studies of benzoxazole and benzothiazole derivatives as VEGFR-2 inhibitors. *Intell. Pharm.* **2024**, *2*, 232–250. [CrossRef]

33. Stielow, M.; Witczyńska, A.; Kubryń, N.; Fijałkowski, Ł.; Nowaczyk, J.; Nowaczyk, A. Bioavailability of drugs: Current state of knowledge. *Molecules* **2023**, *28*, 8038. [CrossRef] [PubMed]
34. Piton, J.; Petrella, S.; Delarue, M.; André-Leroux, G.; Jarlier, V.; Aubry, A.; Mayer, C. Structural insights into the quinolone resistance mechanism of Mycobacterium tuberculosis DNA gyrase. *PLoS ONE* **2010**, *5*, e12245. [CrossRef]
35. Eberhardt, J.; Santos-Martins, D.; Tillack, A.F.; Forli, S. AutoDock Vina 1.2.0: New docking methods, expanded force field, and Python bindings. *J. Chem. Inf. Model.* **2021**, *61*, 3891–3898. [CrossRef]
36. Sharma, S.; Sharma, A.; Gupta, U. Molecular docking studies on antifungal activity of Allium sativum (garlic) against mucormycosis. *Res. Sq.* **2021**. *preprint*. [CrossRef]
37. Pettersen, E.F.; Goddard, T.D.; Huang, C.C.; Couch, G.S.; Greenblatt, D.M.; Meng, E.C.; Ferrin, T.E. UCSF Chimera: A visualization system for exploratory research and analysis. *J. Comput. Chem.* **2004**, *25*, 1605–1612. [CrossRef]
38. Irwin, J.J.; Shoichet, B.K. ZINC: A free database of commercially available compounds for virtual screening. *J. Chem. Inf. Model.* **2005**, *45*, 177–182. [CrossRef]
39. Abraham, M.J.; Murtola, T.; Schulz, R.; Páll, S.; Smith, J.C.; Hess, B.; Lindahl, E. GROMACS: High performance molecular simulations through multilevel parallelism. *SoftwareX* **2015**, *1–2*, 19–25. [CrossRef]
40. Bugnon, M.; Goullieux, M.; Röhrig, U.F.; Perez, M.A.S.; Daina, A.; Michielin, O.; Zoete, V. SwissParam 2023: A web tool for small molecule parametrization. *J. Chem. Inf. Model.* **2023**, *63*, 6469–6475. [CrossRef]
41. Zoete, V.; Cuendet, M.A.; Grosdidier, A.; Michielin, O. SwissParam: A fast force field generation tool for small organic molecules. *J. Comput. Chem.* **2011**, *32*, 2359–2368. [CrossRef] [PubMed]
42. Brooks, B.R.; Brooks, C.L., III; MacKerell, A.D., Jr.; Nilsson, L.; Petrella, R.J.; Roux, B.; Won, Y.; Archontis, G.; Bartels, C.; Boresch, S.; et al. CHARMM: The biomolecular simulation program. *J. Comput. Chem.* **2009**, *30*, 1545–1614. [CrossRef] [PubMed]
43. Abascal, J.L.F.; Vega, C. A general purpose model for the condensed phases of water: TIP4P/2005. *J. Chem. Phys.* **2005**, *123*, 234505. [CrossRef] [PubMed]
44. Bussi, G.; Donadio, D.; Parrinello, M. Canonical sampling through velocity rescaling. *J. Chem. Phys.* **2007**, *126*, 014101. [CrossRef]
45. Parrinello, M.; Rahman, A. Polymorphic transitions in single crystals: A new molecular dynamics method. *J. Appl. Phys.* **1981**, *52*, 7182–7190. [CrossRef]
46. Essmann, U.; Perera, L.; Berkowitz, M.L.; Darden, T.; Lee, H.; Pedersen, L.G. A smooth particle mesh Ewald method. *J. Chem. Phys.* **1995**, *103*, 8577–8593. [CrossRef]
47. Hess, B. P-LINCS: A parallel linear constraint solver for molecular simulation. *J. Chem. Theory Comput.* **2008**, *4*, 116–122. [CrossRef]
48. Sittel, F.; Jain, A.; Stock, G. Principal component analysis of molecular dynamics: On the use of Cartesian vs internal coordinates. *J. Chem. Phys.* **2014**, *141*, 014111. [CrossRef]
49. Papaleo, E.; Mereghetti, P.; Fantucci, P.; Grandori, R.; De Gioia, L. Free-energy landscape, PCA, and structural clustering to identify conformations from MD: Myoglobin case. *J. Mol. Graph. Model.* **2009**, *27*, 889–899. [CrossRef]
50. Kumari, R.; Kumar, R.; Lynn, A.; OSDD Consortium. g_mmpbsa: A GROMACS tool for MM-PBSA calculations. *J. Chem. Inf. Model.* **2014**, *54*, 1951–1962. [CrossRef]
51. Wang, E.; Sun, H.; Wang, J.; Wang, Z.; Liu, H.; Zhang, J.Z.H.; Hou, T. End-point binding free energy calculation with MM/PBSA and MM/GBSA: Strategies and applications. *Chem. Rev.* **2019**, *119*, 9478–9508. [CrossRef] [PubMed]
52. Paul, L.; Shadrack, D.M.; Mudogo, C.N.; Mtei, K.M.; Machunda, R.L.; Ntie-Kang, F. Structural characterization of cassava linamarase–linamarin complex: A computational approach. *J. Biomol. Struct. Dyn.* **2022**, *40*, 9270–9278. [CrossRef] [PubMed]
53. Baum, B.; Muley, L.; Smolinski, M.; Heine, A.; Hangauer, D.; Klebe, G. Non-additivity of Functional Group Contributions in Protein–Ligand Binding: A Comprehensive Study by Crystallography and Isothermal Titration Calorimetry. *J. Mol. Biol.* **2010**, *397*, 1042–1054. [CrossRef] [PubMed]
54. Nguyen, H.D.; Kim, M.-S. Identification of promising inhibitory heterocyclic compounds against acetylcholinesterase using QSAR, ADMET, biological activity, and molecular docking. *Comput. Biol. Chem.* **2023**, *104*, 107872. [CrossRef]
55. Dias, M.V.B.; Vasconcelos, I.B.; Prado, A.M.X.; Fadel, V.; Basso, L.A.; de Azevedo, W.F.; Santos, D.S. Binding of isonicotinyl-NAD adduct to wild-type and isoniazid-resistant InhA: Crystallographic studies. *J. Struct. Biol.* **2007**, *159*, 369–380. [CrossRef]
56. Sucharitha, P.; Ramesh Reddy, K.; Satyanarayana, S.V.; Garg, T. ADMET assessment of drugs using computational tools. In *Computational Approaches for Novel Therapeutic and Diagnostic Designing to Mitigate SARS-CoV-2 Infection*; Academic Press: Cambridge, MA, USA, 2022; pp. 335–355. [CrossRef]
57. Alsenan, S.; Al-Turaiki, I.; Hafez, A. A deep learning approach to predict blood–brain barrier permeability. *PeerJ Comput. Sci.* **2021**, *7*, e515. [CrossRef]
58. Veber, D.F.; Johnson, S.R.; Cheng, H.; Smith, B.R.; Ward, K.W.; Kopple, K.D. Molecular properties that influence the oral bioavailability of drug candidates. *J. Med. Chem.* **2002**, *45*, 2615–2623. [CrossRef]
59. Guterres, H.; Im, W. Improving protein–ligand docking results with high-throughput molecular dynamics simulations. *J. Chem. Inf. Model.* **2020**, *60*, 2189–2198. [CrossRef]

60. Liu, K.; Watanabe, E.; Kokubo, H. Exploring stability of ligand binding modes by molecular dynamics simulations. *J. Comput. Aided Mol. Des.* **2017**, *31*, 201–211. [CrossRef]
61. Cao, X.; Hummel, M.H.; Wang, Y.; Simmerling, C.; Coutsias, E.A. Exact analytical algorithm for solvent-accessible surface area and derivatives in implicit solvent simulations on GPUs. *J. Chem. Theory Comput.* **2024**, *20*, 4456–4468. [CrossRef]
62. Huang, H.; Simmerling, C. Fast pairwise approximation of solvent accessible surface area for implicit solvent simulations. *J. Chem. Theory Comput.* **2018**, *14*, 5797–5814. [CrossRef] [PubMed]
63. Smith, A.; Raghavan, V. Molecular dynamics simulation of the thermal treatment of the Ara h 6 peanut protein. *Processes* **2025**, *13*, 434. [CrossRef]
64. Islam, M.T.; Aktaruzzaman, M.; Barai, C.; Rafi, F.I.; Hasan, A.R.; Tasnim, T.; Sarder, P.; Albadrani, G.M.; Al-Ghadi, M.Q.; Sayed, A.A.; et al. In silico screening of dietary compounds as butyrylcholinesterase inhibitors for Alzheimer's disease. *Sci. Rep.* **2025**, *15*, 17134. [CrossRef]
65. Maruyama, Y.; Igarashi, R.; Ushiku, Y.; Mitsutake, A. Analysis of protein folding simulation with moving RMSD. *J. Chem. Inf. Model.* **2023**, *63*, 1529–1541. [CrossRef]
66. Mascoli, V.; Liguori, N.; Cupellini, L.; Elias, E.; Mennucci, B.; Croce, R. Interactions driving carotenoid binding in light-harvesting complexes. *Chem. Sci.* **2021**, *12*, 5113–5122. [CrossRef]
67. Ragunathan, A.; Malathi, K.; Anbarasu, A. MurB as a target in addressing Vibrio cholerae resistance through docking and MD simulation. *J. Cell. Biochem.* **2018**, *119*, 1726–1732. [CrossRef]
68. Bianco, V.; Iskrov, S.; Franzese, G. Hydrogen bonds in water dynamics and protein stability. *J. Biol. Phys.* **2012**, *38*, 27–48. [CrossRef]
69. Qin, X.; Zhong, J.; Wang, Y. Homology modeling, docking, and MD simulation of a mutant T1 lipase with fatty acids. *J. Biotechnol.* **2021**, *337*, 24–34. [CrossRef]
70. Abdelsattar, A.S.; Mansour, Y.; Aboul-ela, F. Perturbed free-energy landscape: Linking ligand binding to biomolecular folding. *ChemBioChem* **2021**, *22*, 1499–1516. [CrossRef]

Disclaimer/Publisher's Note: The statements, opinions and data contained in all publications are solely those of the individual author(s) and contributor(s) and not of MDPI and/or the editor(s). MDPI and/or the editor(s) disclaim responsibility for any injury to people or property resulting from any ideas, methods, instructions or products referred to in the content.